

ICSO 2016

International Conference on Space Optics

Biarritz, France

18–21 October 2016

Edited by Bruno Cugny, Nikos Karafolas and Zoran Sodnik



Optical models of MXT using Zemax

J. M. Le Duigou

K. Mercier

F. Gonzalez

D. Götz

et al.



icso proceedings



International Conference on Space Optics — ICSO 2016, edited by Bruno Cugny, Nikos Karafolas,
Zoran Sodnik, Proc. of SPIE Vol. 10562, 105620T · © 2016 ESA and CNES
CCC code: 0277-786X/17/\$18 · doi: 10.1117/12.2296139

Proc. of SPIE Vol. 10562 105620T-1

OPTICAL MODELS OF MXT USING ZEMAX

J.M. Le Duigou¹, K. Mercier¹, F. Gonzalez¹, D. Götz², A. Meuris²

¹: Centre National d'Etudes Spatiale
18 Avenue Edouard Belin
31401 TOULOUSE Cedex 9 – France
Tel: (+33) 1 61 28 21 24
Fax: (+33) 1 61 28 26 92

Jean-Michel.LeDuigou@cnes.fr

²: Commissariat à l'Energie Atomique

I. INTRODUCTION

The Microchannel X-ray Telescope (MXT) is a soft X-rays instrument on board SVOM, a Sino French mission. The launch is planned in 2021 by a LM-2C rocket. The main SVOM general objective is the survey of Gamma Ray Bursts, in coordination with ground telescopes. The other main on board instruments are ECLAIR (gamma, french), GRM (gamma, Chinese) and VT (visible, chinese). MXT is based on a cooled silicium based detector, provided by the Max-Planck-Institut für Extraterrestrische Physik (MPE) and encapsulated in a camera developed by CEA, and a set of microchannel plates manufactured by Photonis. These plates are integrated on a mounting frame by the University of Leicester (UoL) to operate like a soft X-ray lens using a “lobster eye” design. The main requirements are a full width half maximum (FWHM) of 4.5 arcmin and an effective area of 30 cm² at 1.0 keV.

In the frame of the French payload phase B, under CNES responsibility, we developed a simplified model of the optics using the Zemax code with customized procedures in non-sequential mode. The computations combine a geometric raytracing with the effects of diffraction and scattering in the pores. After recalling the general description of the instrument and the basic principles of its optics, we present first the simulations of the X-rays and UV PSF in the field of view (FOV). We compare the results with the simulations made by UoL [1]. Then we focus on the straylight analysis and present the design impacts of our simulations.

II. MXT DESCRIPTION

A. General

MXT is a very light (<35 kg), and compact (<1.2 m) focusing X-ray telescope. Its large field of view (1 degree) and its sensitivity below the mCrab level make of MXT a very good instrument to identify and precisely localize (below the arc minute) X-ray transients in non-crowded fields, and to study them in detail, thanks to its excellent spectral response. It is designed to measure from 0.2 to 10 Kev with a maximum sensitivity around 1 keV.

MXT is composed by five main subsystems: an optical module based on square micro-pore optics (MPOs), a camera, a carbon fibre structure, a data processing unit and a radiator (see Fig. 1). A small baffle provides a protection against direct sun illumination. The interface with the satellite is made through 3 fixation zones and a titanium ring. The nominal focal length of the instrument is F=1 m, although studies are going on to increase it to 1.15 m.

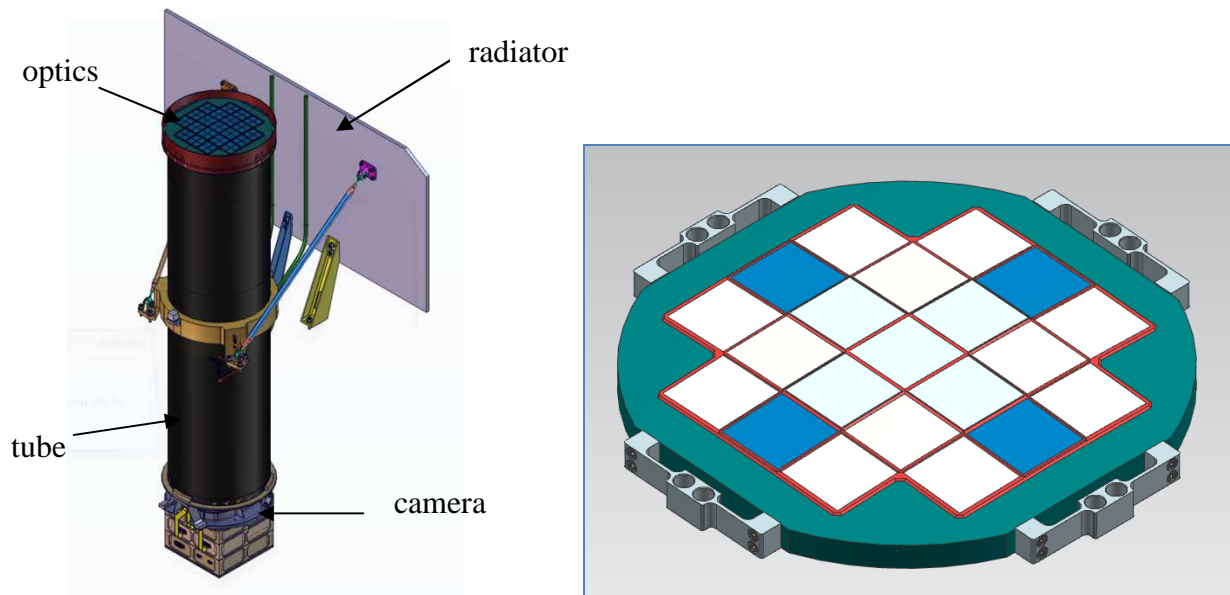


Fig. 1. General view of MXT (left), zoom on the optical module (right)

B. Optics

The optics of MXT is based on a “Lobster Eye” geometry and optimized for a narrow-field use (Fig. 2 left) [2][3]. The rays hit the inner walls of the micro-pores with grazing incidence. The pores are square with $d=40\ \mu\text{m}$ size and a pitch of $p=52\ \mu\text{m}$. The inner walls are coated with a 25 nm Ir layer to boost the reflectivity. The pores are grouped in plates of 40 x 40 mm side (600625 pores). 21 of them are used to full the aperture (Fig. 1, right). Their thickness is optimized to avoid vignetting and maximize the effective area. The central plates have $L=2.4\ \text{mm}$ thickness while the outermost ones have $L=1.05\ \text{mm}$. They are bonded on an aluminum frame which upper face is a sphere of radius 2000 mm, with 10 μm machining precision. The MPO are covered with a 70 nm Aluminum film to avoid thermal flux and straylight from entering the instrument.

The Point Spread Function (PSF) has a peculiar form, and is composed by a central spot and two cross arms (Fig. 2, right): X-rays entering in the MPOs can either be reflected twice and focused in the central PSF spot, or reflected just once and focused in the PSF arms. For MXT about 50% of the incident X-ray flux is focused in the central spot, 2 x 22% in the arms, and the rest in a diffuse patch. Thanks to the “Lobster Eye” geometry the vignetting is very low, of the order of 10-15% at the edge of the FOV.

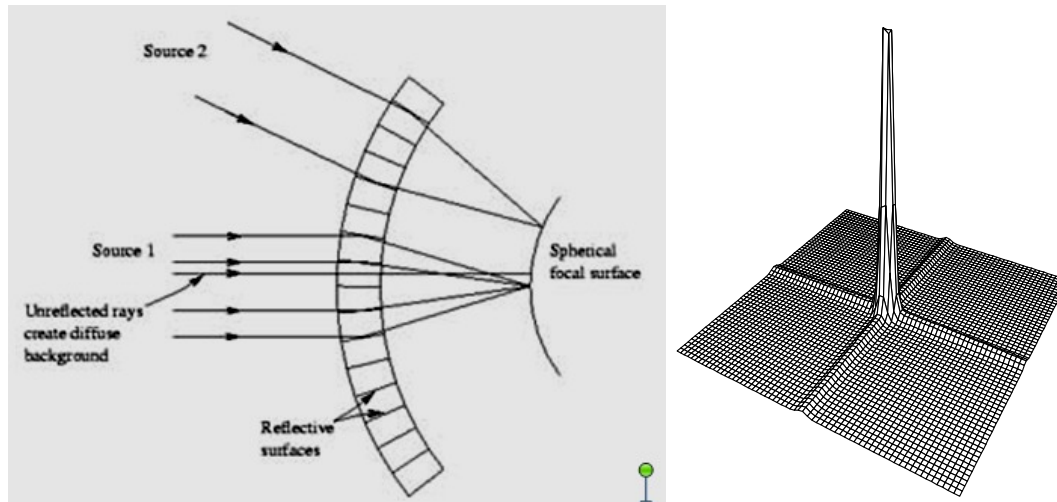


Fig. 2. Principle of focusing with the “lobster eye” design (left), shape of the PSF (right)

C. Camera

The PSF is imaged on a Silicon based pnCCD having 256 x 256 75 μm side pixels associated with a front-end electronics (FEE) based on two CAMEX. It is fully depleted (450 μm depth) and has excellent low-energy response (45-48 eV (FWHM) @ 277 eV), and energy resolution (123-131 eV FWHM @ 5.9 keV). The spatial sampling is good enough to avoid any degradation of the PSF. The CCD is thermally controlled by 3 TEC at -65°C (to reduce noise) with a daily stability better than $\pm 1^\circ\text{C}$. The CCD is covered by a 100 nm Aluminum layer to protect against UV/Visible straylight because the CCD is still sensitive in this spectral range. This results in a slight transmission loss in the X-ray range. It is also protected against background X-rays by an aluminum shielding. A filter wheel can put various filters in front of the CCD and its entrance cone. The external box of the camera provides the interfaces with the radiator, the front end electronics and the tube (Fig. 3).

With a 1.0 m focal length, each pixel corresponds to 15.4 arcsec. The FOV is in practice limited by the CCD and is a 57 x 57 arcmin square. At 20 arcmin FOV radius the vignetting factor is greater than 0.9.

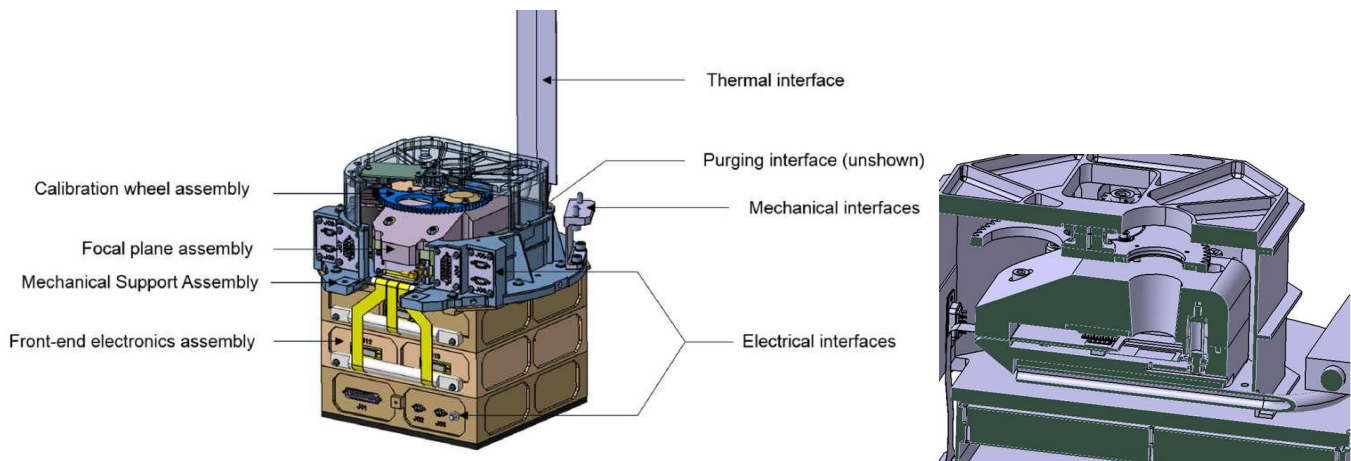


Fig. 3. Camera layout

The instrument effective area is a combination of the optics effective area, the transmission of the aluminum filters, the size of the CCD and its quantum efficiency.

III. X-RAY AND UV PSF

A. X-RAYS

The PSF at the center of the FOV was extensively studied by UoL with a dedicated software [1]. We report here a comparison of what we obtained with Zemax in a simplified manner.

Modeling in Zemax

Zemax is a general optical software widely used in the world and which benefits from a high level of validation. It can be used to model small wavelengths provided the objects are not too small ($>10 \lambda$) and the index data are available. For this last point, we used the database of the Center for X-Rays Optics (CXRO). The size of the pores and of the wedges between them (few μm to tens of μm) is much larger than the criteria of 10λ (here typically 10 nm).

The glass used for the MPO has a high density. Hence, in the soft X-rays range, even a small thickness of glass is enough to stop rays. This allows to consider only reflected rays and to use traditional ray tracing in a quite simple manner.

In non-sequential mode (NSC), Zemax assumes that all the objects are defined before launching the rays. The basic element we use is an “extruded object”. By defining a section and stretching it along one direction, Zemax can represent this way pores or group of pores. As it is impossible to represent simultaneously the ~ 12 million pores involved in MXT optics, the way to proceed is to represent a small subset of pores, launch rays for this subset, measure the energy on a detector, move the subset onto the aperture and cumulate the energy deposited on the CCD. The programming of this loop can be done using the ZPL language and dedicated macros. The spherical geometry of the “lobster eye” is quite easy to implement. Various manufacturing errors can be introduced at the subset level, like an orientation error or a pore shape error. Performing this process with a subset of 1 pore is much too fine and takes a too long time to simulate. We found that using a 5×5 pores subset (see Fig. 4), with uniform manufacturing errors at this scale, was a good compromise between computation time and representativeness of the geometry. 25 of this objects forms a multifiber (25×25 pores).

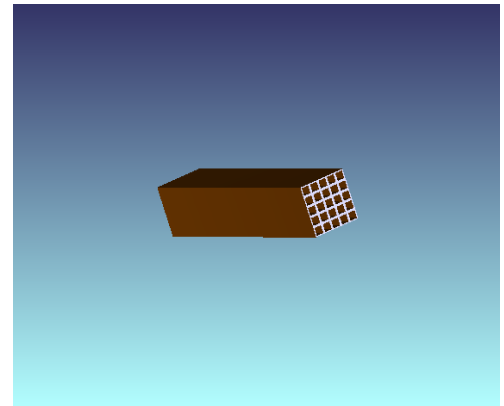


Fig.4: 5 x 5 pores extruded object

The number of rays to launch plays an important role. To avoid excessive time computation one has to use the minimum number of rays to correctly represent the PSF. We performed some tests with increasing number of rays and we found that having 10 to 100 rays for one multifiber (625 pores) was sufficient to have better than 1% precision results. The source object is just a rectangle, the size of a multifiber.

The reflectivity of the 25 nm Ir layer is modelled with tabulated data from CXRO database (angle, wavelength) assuming a roughness of 1.3 nm rms (Fig. 5, left). The 70 nm aluminium film in front of the MPO plays a role in the effective area, so its transmission as to be taken into account (fig. 5, right, CXRO database).

The detector is modelled simply as an array of 256×256 $75 \mu\text{m}$ size pixels.

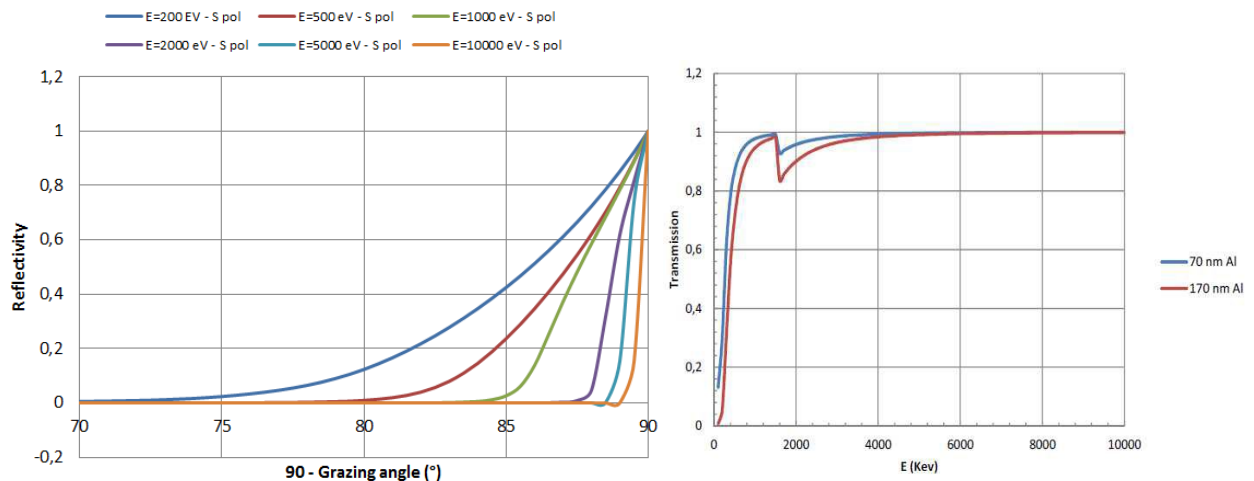


Fig. 5. Iridium reflectivity from CXRO for various energies (left) and transmission of a thin Al film (right)

Perfect geometry and pores

Assuming perfect pores and a perfect geometry, the FWHM of the PSF central spot is limited by three aberrations:

- Spherical aberration: $\Delta\theta_s = 4 \sqrt{2} (d/L)^3$
- Diffraction: $\Delta\theta_d = 2 (\lambda/d)$
- Geometric pore size: $\Delta\theta_g = d/F$

For the adopted MXT parameters, the three aberrations have approximately the same value, 10 arcsec.

MPO manufacture errors

In the end, the FWHM is not dominated by these factors but by the manufacturing errors which lead to imperfect geometry and limit the FWHM. The two most important ones are the pore shear and the pore alignment errors. The first one is a distortion of the pore shape from a square to a parallelogram (angle θ_h). It is introduced when the square flat MPO is slumped onto a spherical tool under pressure. It is more important in the corners of a MPO plate than in the center. The pore alignment error (angle θ_a) is induced by the stacking process or the slumping. The axis of the pores is no more aligned with the normal to the spherical surface, deviating the output rays with an angle twice that of the alignment error. Another important error is the pore figure error (angle θ_f): the inner walls of the pores are not perfectly flat but have low order wavefront errors (WFE) which depend mainly on the etching process. The effect of θ_a and θ_f overlaps and are not easily separated. Typical values from UoL are $\theta_h = 0.3^\circ$ and $\theta_{af} = 0.75$ arcmin [1] [5].

In our simulations we assumed that θ_h is constant over one MPO and θ_{af} can be represented by a gaussian error with 0.75 arcmin rms standard deviation. No finer dependence of these errors with the position in one plate (corner / edge / center) has been taken into account. The typical effect of the shear error is found (fig 6, left): the main peak is split into four smaller peaks. Cumulating all the errors (Fig 6, right), we found a 4.1 arcmin FWHM to be compared with the 4.4 arcmin of UoL. These results are in good agreement given the simplifications we made.

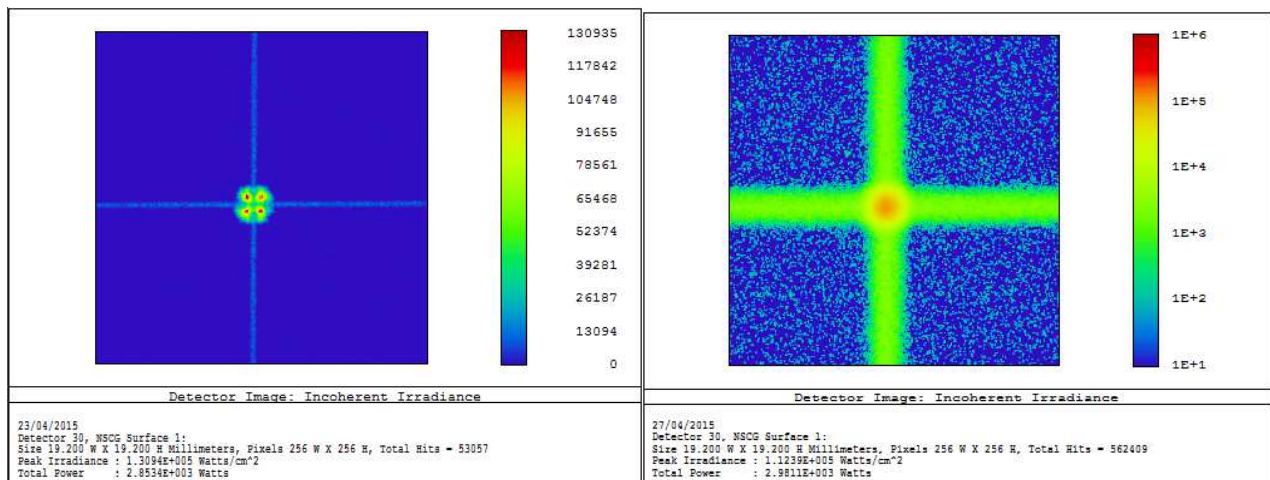


Fig. 6. Effect of pore shear ($\theta_h=0.6$, left), full PSF simulated with $\theta_h=0.3$, $\theta_{af}=0.75$ arcmin rms

The effective area could also be computed at various energies and is compared with the UoL data on Fig. 7 (left). The Zemax results fit reasonably well with UoL data within a 10-15% precision.

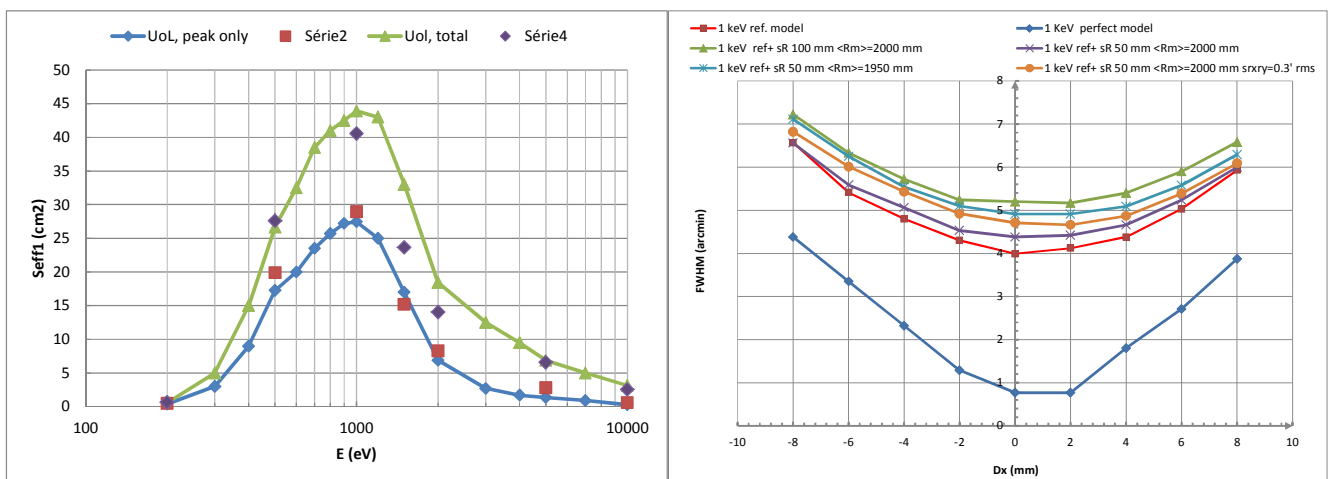


Fig. 7. Left: Simulated effective area of the instrument for $\theta_h=0.3$, $\theta_{af}=0.75$ arcmin rms. In green, total effective area, in blue, central spot only. Red squares and purple diamonds are the Zemax simulation. Right: impacts of assembly errors on the defocus curve. The reference model is with $\theta_h=0.3^\circ$, $\theta_{af}=0.75$ arcmin rms. sR is the standard deviation of the MPO radius, $\langle R_m \rangle$ is its averaged value. srxry is the standard deviation of the tip/tilt error of the MPO mounted on the frame.

In the previous sections, the MPO were supposed to be mounted on the supporting frame without error. Here we take into account possible tip/tilt errors, as well as a dispersion of the radius of curvature of the MPO plates, on top of the manufacture errors. The impact of these defaults is plotted on the defocus curve (Fig. 7, right). We see that for keeping a FWHM close to the requirement, we need first to set the radius of curvature of the frame to the average value of the MPO radius of curvature. The standard deviation of the MPO radius of curvature has to be less than 50 mm rms. Furthermore the tip/tilt errors have to be lower than 1 arcmin 3σ . (0.3 arcmin rms). This is well in line with the 10 μm accuracy of the frame spherical surface: 10 μm over 40 mm side is ~ 50 arcsec.

B. EUV

The aluminium film on the MPO has a transmission window in the extreme UV (EUV) spectral range (see Fig. 9). For the GRB localization, this could be a problem if bright sources are in the vicinity because of the induced noise. That's why we studied the optical response in this range. The previous computations performed in X-rays can be extended in the EUV range, but the diffraction has now to be taken into account as the diffraction angle is $\Delta\theta_d = 3.4$ to 8.6 arcmin when λ varies from 40 to 100 nm. One way to put diffraction in Zemax NSC mode is to use a diffractive source instead of a normal one. Unfortunately this only works for simple source shapes, like a square. The previously described computation procedure can be adapted, but using a single pore as a basic object and taking advantage of MPO symmetries. This lead to quite high computation time on a standard PC (few days) but remains feasible if not too much runs are required. The scattering is not taken into account directly, but the reflection coefficients computed in the CXRO database are taken with 1.3 nm rms roughness (at 40 nm, supposed constant up to 80 nm).

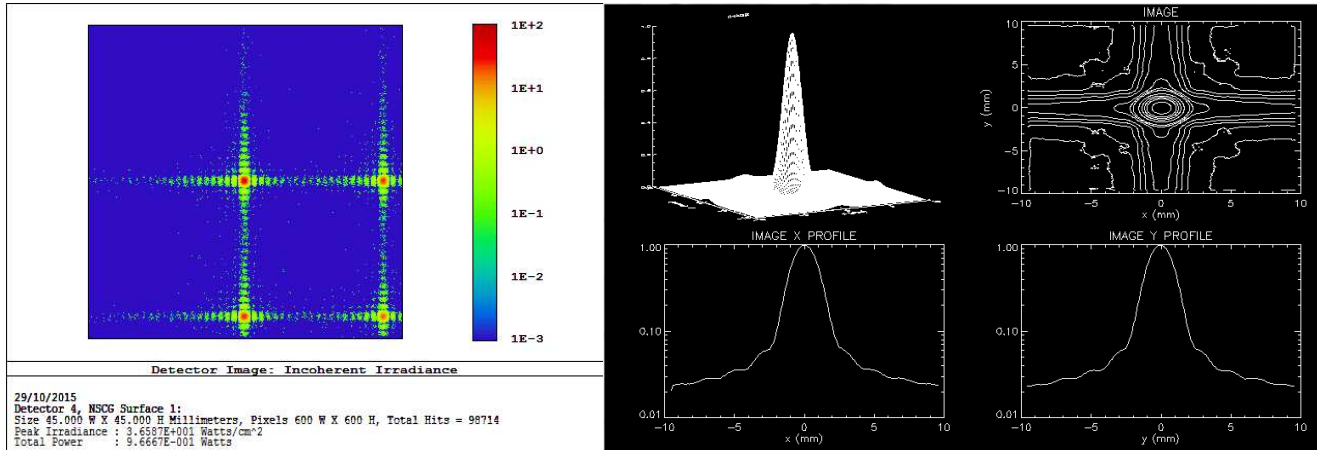


Fig. 8. Left: EUV simulation on one pore with characteristic diffraction effect of a square pore aperture. Right: PSF simulation for 21 MPO at $\lambda=80$ nm with $\theta_h=0.3^\circ$, $\theta_{af}=0.75$ arcmin rms, $srxry=0.3'$ rms.

Fig. 8 shows the diffraction of one pore (left) and the simulated PSF for the full aperture at 80 nm including manufacturing errors (right). We found that the FWHM is 5.1 arcmin at 40 nm and 7 arcmin at 80 nm. It is very close to a quadratic sum of the FWHM without diffraction and the $\Delta\theta_d$ value. The effective area of the central spot without the Al transmission is close to 43 cm^2 (Including 170 nm Al transmission, we have 28 and 6 cm^2 at 40 and 80 nm).

So MXT forms focused images of EUV sources, with a significant effective area and with a FWHM enlarged by the diffraction. At higher wavelength (> 200 nm), the diffraction dominates and becomes huge so that no focused image is formed. Estimations show that a G2V star at 100 pc (EUV flux in [6]) leads to $0.6 \cdot 10^{-5}$ e-/px/0.1s. For a O9V star at 300 pc [7], we get 3800 e-/px/0.1s. In some cases, bright EUV sources in the FOV could be a problem for MXT if it is used to point in too crowded areas. A dedicated filter will be placed on the filter wheel.

IV. STRAYLIGHT ANALYSIS

As the CCD is sensitive up to 1.1 μm , MXT can be affected by straylight coming from the sun, the moon or the earth. The maximum level allocated for the straylight is 1 e-/px/0.1s (one MXT frame is 0.1 s) equivalent to $1.8 \cdot 10^5$ e-/ cm^2/s when dealing with an average flux on the CCD. The most demanding criteria is the spectral resolution of the instrument (75 eV).

A. CCD response

The conversion of photons into electrons is made using the product $\eta_q = G_{si} \times G_q$ using values in table 1 (CEA data).

B. MATERIAL PROPERTIES

The measured transmission of a 150 nm layer of Aluminum (Fig. 9, left) is taken from [4]. An extrapolation was made for 70 and 100 nm layer. The Iridium index is known from various sources on the refractiveindex.info database (Fig. 9, right).

Spectral band	G_{Si} (no unit)	G_Q (e-/photons)	η_Q (e-/photons)
20-100	1	17	17
100-200	1	3	3
200-300	1	2	2
300-400	1	1	1
400-500	0.93	1	0.93
500-600	0.87	1	0.87
600-700	0.8	1	0.8
700-900	0.73	1	0.73
800-900	0.67	1	0.67
900-1000	0.6	1	0.6
1000-1100	0.5	1	0.5

Table 1: quantum efficiency and conversion factor of the CCD

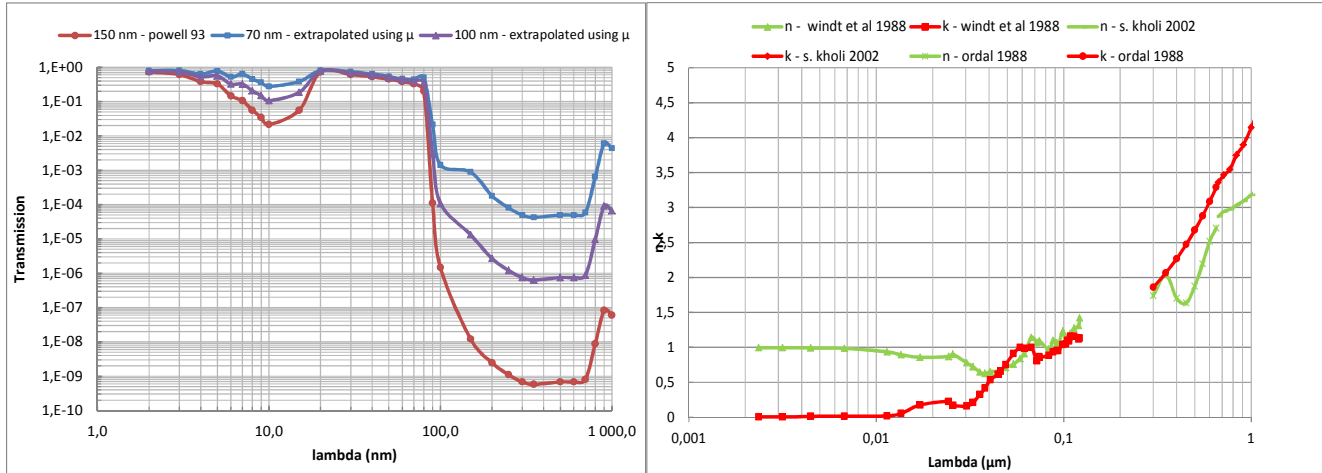


Fig. 9. Left: Transmission of Aluminium thin layers. Right: complex index of iridium.

The exact composition of the MPO glass is not known. We took LF5 as an equivalent (same density). This is only to model how the rays propagate between the pores in the visible.

C. DIFFUSION

In the EUV range, the scattering in the pores is likely to be dominated by the roughness, assumed to have the nominal value 1.3 nm rms. The adopted Bidirectional Reflectance Distribution Function (BRDF) at 60 nm is an ABg model with $A=4.8 \cdot 10^{-4}$, $B=10^{-5}$ and $g=2.6$ (TIS=0.074).

In the visible, the scattering in the pores will be dominated by contamination. The level of contamination of MXT is expected to be 1000 ppm. We will consider a somewhat broader BRDF: $A=3.5 \cdot 10^{-4}$, $B=6.510^{-4}$ and $g=1.6$ (TIS=0.004). It is assumed to be constant from 300 nm to 1100 nm.

These BRDF are not valid for grazing angles, but only for local incidence angles from 0 to 60°.

The tube inner walls and the camera cover are all supposed to be painted with a space compatible very diffusive black paint (PNC). From measurement at CNES, the total reflectivity is 3% assumed constant in the spectral range of interest and the diffusion law is Lambertian.

D. MXT PST

We studied the point source transmission (PST) of MXT at two wavelengths only, as this is a complex and time consuming task. We selected 60 nm because it is the center of the Aluminum transmission window in the EUV and 550 nm to represent the visible spectrum. The full PST is a combination of the 21 MPO's filtering, with different thickness and position, and the properties of the optical cavity behind them. The square geometry of the pores implies that no full axial symmetry exists. The transmission of one pore requires two angles to be described correctly: the incidence angle i (wrt to pore axis) and an azimuth angle ψ (see Fig. 10). The entrance cone of the camera and its cover (see Fig. 3) were taken into account as well as the geometry of the tube. The back of the optics is assumed to be a semi-reflective surface (0.5 reflection coefficient).

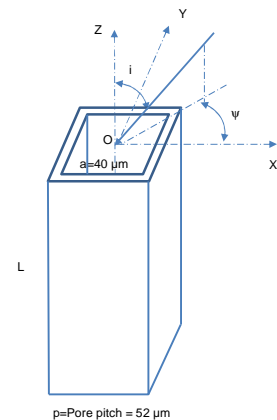


Fig.10: pore geometry

EUV

In this range, the glass totally absorbs the rays propagating between the pores. This simplifies the problem. Only specular or diffused rays inside the pores reach the output. The greater the incidence, the higher the number of reflexions, the lower the part of the specular rays in the output energy of one pore, the more diffused light dominates. Fig. 11 (left) illustrates the distribution of the light at the output of one pore. For low i ($<20^\circ$), the output pattern is dominated by 2 to 4 peaks with directions corresponding to i, ψ . The diffused light forms a halo around them. For higher i ($>30^\circ$), the contribution of these peaks tends to disappear and the diffused light dominates. The output pattern is then quite constant with i and ψ with a diamond like shape. The light coming out of the pore either strikes the CCD directly going through the entrance cone in the camera (see Fig. 3) or indirectly via the diffusion on the tube walls. More complex paths involving the back of the optics are of lesser importance. The transmission from pore entrance to CCD, for different pore thickness is illustrated on Fig. 11 (right) for $\psi=0$. It goes down quite linearly up to $i=30^\circ$ and reaches a plateau after that. The level depends on the thickness of the pores.

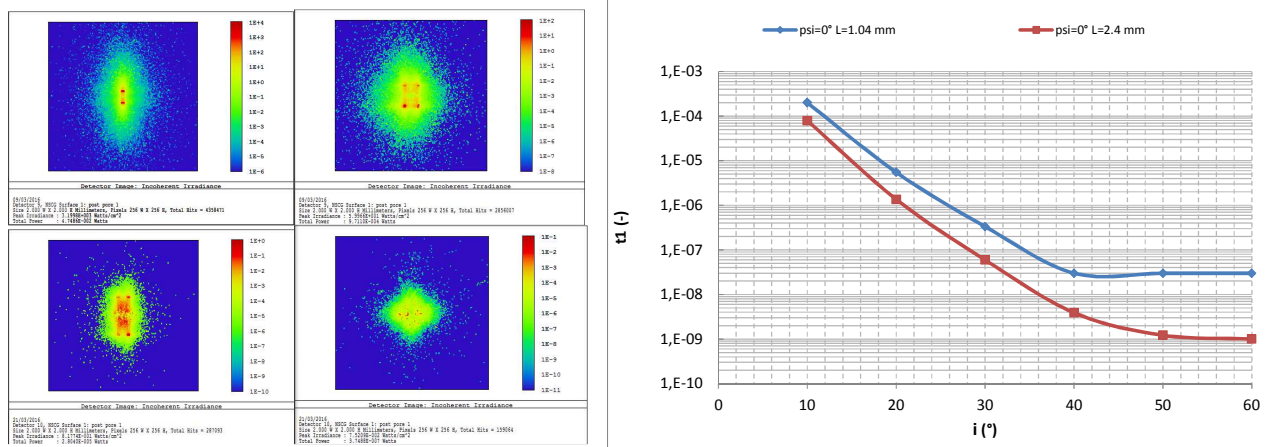


Fig. 11. Left: light distribution at pore outputs, $\lambda=60$ nm, $i, \psi = (10,0), (20,30), (30,20), (60,45)$. Right: PST at $\lambda=60$ nm, $\psi = 0$

Visible

In the visible, the situation is more complex as the rays may propagate in the glass between two pores. One has then to take into account not only one pore but also its neighbors. Tests show that taking into account a set of 11×11 adjacent pores is precise enough. Like in the UV range, the output light can either hit directly the CCD or have first a reflection on the tube walls. For low i and ψ , the light is dominated by indirect paths on the tube walls with specular directions out of the pores. The transmission decreases almost linearly with i and ψ . In this case, a longer pore leads to a lower transmission. For high i , the transmission is nearly constant and has low dependence on ψ and L . This is consistent with a light dominated by scattered rays in the pores finding a direct path to the CCD.

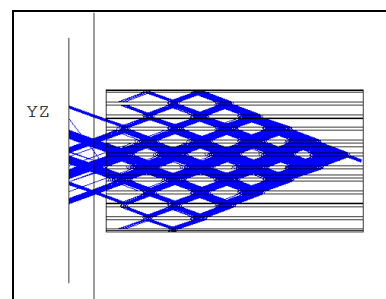


Fig.12: lights propagating in adjacent pores, $\lambda=550$ nm

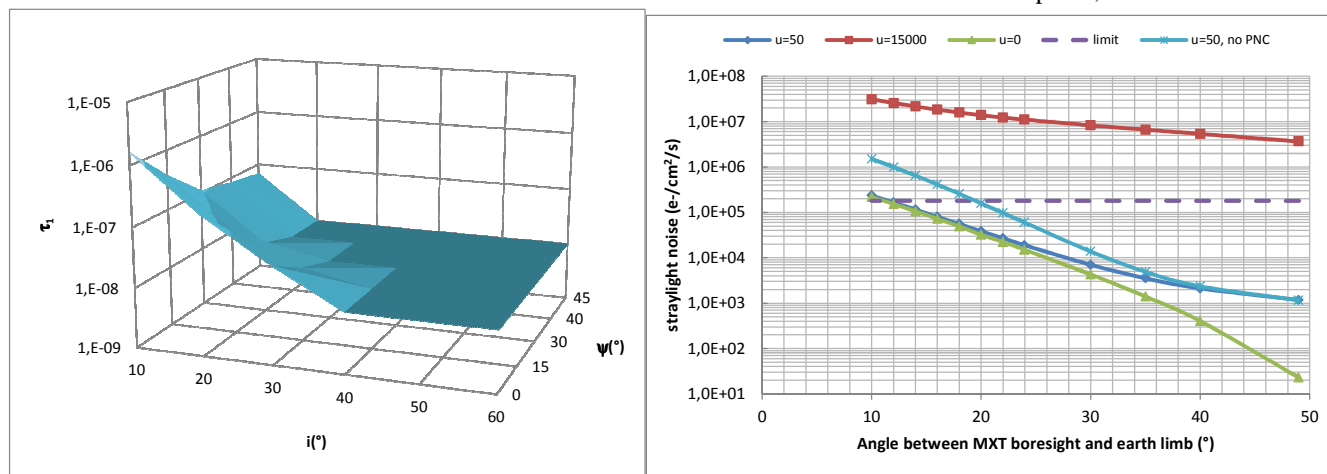


Fig. 13. Left: PST of full optic, $\lambda=550$ nm. Right: noise level of earth straylight as a function of guard angle

The PST of the full optic was computed taking only one pore per MPO (11×11 set of pores), assuming the transmission from pore entrance to CCD is constant within one MPO. The obtained 2D function is illustrated by Fig. 13 (left).

E. RESULTS

Earth

The earth is the main optical straylight source for MXT. The important parameter to study is the guard angle between the instrument boresight and the earth limb, as this is an operational constraint for the mission. The current proposed value is 20° , derived from the SWIFT mission. As the satellite altitude is about 600 km, MXT has potentially a large portion of the earth in its field of view. Using the PST previously computed, the orbital parameters, the earth flux from SPOT satellites data and [8] for UV earth albedo, a 2D integral over the portion of earth having a factor of view with the optic entrance pupil can be computed numerically. It is multiplied by the transmission of the 70 nm film (t_{70}), including the $1/\cos i$ effect on the thickness, the transmission of the 100 nm coating on the CCD (t_{100} , see Fig. 9) and the efficiency η_q of the CCD (table 1). t_{70} includes a fraction u of “open” pores per MPO with unity transmission. They results from defaults in the aluminum film and depressurization during the launch. The current requirement is $u=50$.

With the baseline design (dark blue curve, diamond), the noise limit is reached at 12° angle. For this value, the integral is dominated by a small area of the earth with the minimal incidence angles on the optics (i ranging from 10 to 25°). At 20° angle the margin is quite good (factor of 5). For low guard angles, the dominating paths to the CCD are the specular rays out of the pores hitting indirectly the CCD after reflection on the tube walls. When increasing the guard angle, the portion of the earth seen by the optics decreases. The incident power on the optics decreases from 8.3 to 2.3 W when varying from 10 to 40° . Also, the average incidence angle increases, hence the collecting area decreases with $\cos i$. The integral is less dominated by a small area. The scattered rays in the pores with direct path to the CCD dominate more. Spectrally, the noise is dominated by near IR because of the increasing transmission of the Al film in this range (see Fig. 9), despite the low energy of the photons.

Assuming a perfect Al film ($u=0$), we have the green (triangle) curve. There is not much difference for low guard angle because in this case the dominating portion of the earth is seen from the optics with a quite low average incidence angle and for $u < 100$ and $i < 40^\circ$, the t_{70} transmission in IR is not very sensitive to u . Assuming $u=15000$ (this corresponds to a 0.25 mm strip of uncovered pores at the edge of a MPO), we get the red (square) curve. No matter the guard angle is, the limit is overcome with more than 1 order of magnitude. Removing the diffusing paint inside the tube with only raw CFRP (light blue, stars) leads to an increase for low guard angle because it affects the indirect paths dominating in this region. The limit in this case is 20° but without margin.

Moon

We took into account the reflected light of a full moon with a constant albedo of 0.04. The resulting effect is negligible and the guard angle can be decreased down to 10° safely.

Sun

Due to the payload layout and the mission in orbit planning, the sun can never be above the plane of the aperture. As the lens is not flat, we just have to protect it by a small baffle of >12 mm height. As the radiators and the other instruments are lower than the aperture plane, we don't have to consider reflections on them.

V. CONCLUSION

Using Zemax, we could model the in FOV X-rays properties of MXT optics. The obtained results are well in line with the UoL predictions using the state of the art for manufacturing errors: 0.75 arcmin for pore alignment/figure error and 0.3° for the shear error. We find that during assembly of the MPO on the frame, tip/tilt errors shall be lower than 1 arcmin. Furthermore, the standard deviation of the MPO radius of curvature shall be less than 50 mm rms. The optics also forms an image in the EUV range but it is enlarged due to diffraction. As the collecting area is not negligible, care as to be taken with bright sources in the FOV while detecting a GRB. A dedicated filter is implemented on the wheel. The straylight analysis shows that the sun is not a problem because the radiator and the other instruments are lower than the aperture. The moon has a negligible effect and could be as close as 10° from the instrument boresight. The earth will be the dominating straylight source in the visible/IR. The 20° guard angle is safe with a quite good margin. Given the many uncertainties of our computations it is not possible to lower this limit. The tube inner walls shall be covered with a diffusive black paint. No long baffle is required, only a short one to prevent the sun from hitting directly the optics in some rare cases. Further work will include a more precise model of the various errors, especially the recently measured distortions occurring at the multifiber interfaces, and test on samples to validate the models.

REFERENCES

- [1] R. Willingale, “Lobster eye optics”, World Scientific Review – dec. 2014.
- [2] R. Willingale, G. Fraser, “Hard X-Ray imaging with microchannel plate optics”, in *Experimental Astronomy*, 8: 281-296, 1998.
- [3] J.R.P Angel, “Lobster eye as X-ray telescope”, *The Astrophysical Journal*, 233:364:373, 1979
- [4] F.R. Powell, “Transmittance measurements for a variety of x-ray/EUV filter materials and pinhole leak measurement”, *SPIE*, VOL. 2011, 1993.
- [5] G.J. Price, “Microchannel plate in astronomy”, thesis UoL 2001
- [6] J. M. Fontenla, “High-resolution solar spectral irradiance from extreme ultraviolet to far infrared”, *JOURNAL OF GEOPHYSICAL RESEARCH*, VOL. 116, D20108, 2011
- [7] A. W. A. Pauldrach, “Hot Stars:Old-Fashioned or Trendy?”, *Reviews in Modern Astronomy* Vol. 16 – 2002
- [8] J.E. Frederick, “The ultraviolet albedo of planet earth”, *Tellus B*, August 1987.